

Plasmon-Driven Photocatalysis Leads to Products Known from E-beam and X-ray-Induced Surface Chemistry

Journal Article

Author(s):

Szczerbiński, Jacek; Gyr, Luzia; Kaeslin, Jérôme; Zenobi, Renato 

Publication date:

2018-10-02

Permanent link:

<https://doi.org/10.3929/ethz-b-000300391>

Rights / license:

In Copyright - Non-Commercial Use Permitted

Originally published in:

Nano Letters 18(11), <https://doi.org/10.1021/acs.nanolett.8b02426>

Supporting Information for

**Plasmon-driven photocatalysis leads to products known
from e-beam and x-ray-induced surface chemistry**

Jacek Szczerbiński, Luzia Gyr, Jérôme Kaeslin and Renato Zenobi*

Department of Chemistry and Applied Biosciences, Laboratory of Organic
Chemistry, ETH Zurich, 8093 Zurich, Switzerland,

e-mail: zenobi@org.chem.ethz.ch

Table of Contents

S1. Materials and Methods	2
S2. Temperature programmed desorption mass spectrometry (TPD-MS) measurements.....	4
S3. Measurement of the temperature in the hot spot.....	12
S4. Fermi-Dirac vs. Boltzmann distribution	14
S5. Identification of fluctuations in SER spectra.....	17
Further Supporting Figures	24

S1. Materials and Methods

TERS measurements. We used top-illumination tip-enhanced Raman spectroscopy (TERS) with silver tips in scanning tunneling microscopy (STM) feedback. Low bias voltages (0.1 V) and low current set points (0.1-0.5 nA) were applied to avoid perturbations of the investigated system by the tunneling electrons. More details on the experimental setup can be found in previous reports from our group^{1,2}. Silver tips were etched according to the protocol described in ref. ³. The sample heater was acquired from NT-MDT Spectrum Instruments (Limerick, Ireland) as an accessory for the Ntegra Spectra atomic force microscope.

TER spectra were acquired on 10 pixel \times 10 pixel grids cast over 1 $\mu\text{m} \times 1 \mu\text{m}$ regions on the sample, with a scan rate of max. 0.2 lines/s. The exposure time t was 1-3 seconds for the Stokes measurements (Fig. 2, 4, 5) and was set to between 0.8 and 8 s for the Stokes and anti-Stokes measurements (Fig. S18), in order to maintain a constant signal-to-noise ratio of the spectra. We assumed that the signal-to-noise ratio is proportional to $P \cdot \sqrt{t}$ and adjusted t to the laser power P .

SERS measurements. Surface-enhanced Raman (SER) spectra presented in Fig. S11-S15 and Fig. 5C (fluctuation statistics) were acquired on 20 pixel \times 20 pixel grids (for benzyl mecaptan – BM) or 16 pixel \times 16 pixel grids (for thiophenol, benzeneselenol and biphenyl thiol – BPT) cast over 5 $\mu\text{m} \times 5 \mu\text{m}$ regions on the sample surface, for sample temperatures between 295 and 413 K. Hence, every data point in Fig. 5 (blue marks) is comprised of 400 (or 256) spectra measured at different locations on the SERS substrate. The spectra were acquired for 1 s at a laser power of 140 μW for BPT and benzeneselenol, and 76 μW for thiophenol and BM.

SERS spectra underlying Fig. 5B (SERS signal decay upon desorption) were acquired separately, with 10 pixel \times 10 pixel grids cast over 4 μm \times 4 μm regions. The integration time was 0.5 s, and the laser power was 38 μW . The smaller number of spectra and the shorter acquisition time resulted in a shorter duration of the measurement series: approx. 40 minutes compared to 2.5-3 hours for the fluctuation statistics.

SERS spectra presented in Fig. 3C&E were recorded with laser powers from 0.036 to 2.880 mW. The integration time was set to 0.895-8.000 s in order to maintain a constant signal-to-noise ratio of the spectra.

Confocal Raman measurements. Confocal Raman spectra of bulk thiols, polycyclic aromatic hydrocarbons (PAHs) and carbon nanopowder were acquired utilizing the same instrument as for the acquisition of the SER and TER spectra. The laser power measured on the sample was 2.22-2.88 mW, and the integration time was 10-100 s.

Substrates. Template-stripped gold substrates were used for TERS, according to the protocol by Weiss *et al.*⁴, and following our previous works⁵. The substrates were prepared using EPO-TEK 377 glue or Norland Optical Adhesive No. 61. The EPO-TEK glue was used for the BPT samples, due to its insolubility in N,N-dimethylformamide (DMF) within <2 weeks after preparation of the substrates. The Norland glue was used for all other samples. SERS substrates (Au) were acquired from Silmeco (Copenhagen, Denmark). Substrates for TPD-MS experiments were prepared by thermal evaporation of 2 nm of Ti and 10 nm of Au onto glass cover slides (24 \times 24 mm, Menzel Gläser). Prior to loading into the evaporator (BAL-TEC MED 020), the cover slides were sonicated in ethanol for 15 minutes, immersed in piranha solution for 30 minutes, rinsed with water and

ethanol, and dried with nitrogen. During evaporation the base pressure was approx. 5×10^{-7} mbar.

Samples. Self-assembled monolayers (SAMs) of thiolates were prepared by overnight incubation of gold substrates in 5 mM ethanolic solutions of thiophenol (99+%, Acros Organics), benzyl mercaptan (BM, $\geq 99.0\%$ GC, Fluka), benzeneselenol (97%, Aldrich), 1-hexadecanethiol (HDT, $\geq 99.0\%$, Aldrich) and 1-decanethiol (95+%, ABCR). Samples of 1H,1H,2H,2H-perfluorodecane-1-thiol (PFDT, $\geq 99.0\%$, Apollo) were immersed for 1 h. After incubation the samples were rinsed with copious amounts of ethanol, dried with nitrogen, and investigated immediately. Biphenyl-4-thiol (BPT, 97%, Aldrich) SAMs were prepared with a 5 μ M solution of BPT in DMF (99.8%, extra dry, Acros Organics). BPT samples were rinsed with DMF first, and then with ethanol.

For the measurement of confocal Raman spectra of PAHs, we chose phenanthrene ($\geq 97\%$ HPLC, Fluka), pyrene ($\geq 98\%$, Chem Service), naphthalene (for synthesis, Merck), 1-methyl-1-cyclohexene ($\geq 95\%$ GC, Fluka), fluorene ($\geq 98\%$, Aldrich), anthracene ($\geq 99\%$, Fluka), pentamethylbenzene ($\geq 97\%$ GC, Fluka) and dicyclopentadiene ($\geq 96\%$, Aldrich). Carbon nanopowder ($\geq 99\%$) was purchased from Aldrich.

S2. Temperature programmed desorption mass spectrometry

(TPD-MS) measurements

Active capillary plasma ionization was used in this study, as it is a sensitive ionization technique for polar and non-polar compounds (including perfluorinated compounds), which allows identification of the species desorbed from the sample surface under atmospheric pressure⁶⁻⁸. The plasma source is based on the principle of dielectric barrier discharge and consists of two

electrodes that are separated by a glass capillary. A sine-modulated high voltage (2.3 kVpp, 47 kHz) was applied to the outer electrode while the inner electrode was grounded. The desorption chamber was flushed with nitrogen gas (1.3 L/min), which was also used as carrier and discharge gas. The plasma source was directly connected to the LTQ Orbitrap mass spectrometer (Thermo Fischer Scientific) allowing a 100 % transport efficiency of the ions. Mass spectra were acquired in positive ion mode with a resolution of 30 000 (m/z 400) and with a mass range of 50–500, except for 1H,1H,2H,2H- perfluorodecanethiol and decanethiol where a wider mass range of 50–800 was used.

The desorption chamber for TPD-MS measurements was made of copper, with a 200 W heating cartridge inserted 5 mm below the sample and a thermocouple fixed 3 mm below the sample (Figure S1). The temperature was ramped between 296 and 523 K (or 573 K for HDT and thiophenol) with a rate of 0.53 K/s. In order to avoid sample cooling by the flow of nitrogen, the gas was preheated by flowing through approx. 15 cm of channels inside the copper block before reaching the sample (flow marked in Fig. S1C). The accuracy of the temperature measurement was validated using an IR camera and a leaf-type thermocouple (SA1XL, Omega Engineering GmbH) strapped to the surface of a test sample. The chamber was directly attached to the ionization source.

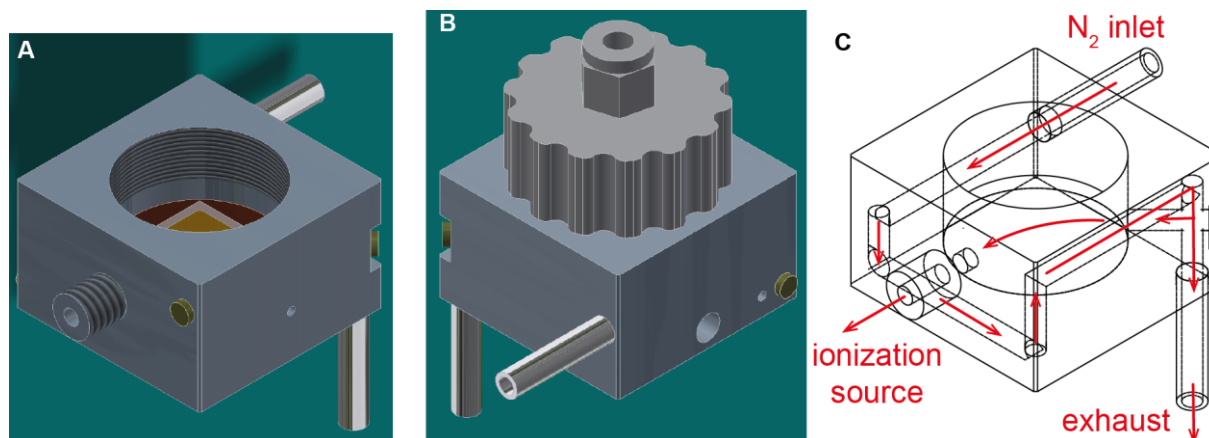


Figure S1. Technical drawings of the desorption chamber used for TPD-MS. (A) The sample (thiolate SAM on a gold coated cover slide) is placed on the bottom of the chamber, directly on the copper surface. (B) The chamber is closed by a titanium screw cap with a rubber seal. (C) The chamber is flushed with nitrogen during the measurement. Before reaching the sample, the gas is preheated by flowing through channels inside the copper block (red arrows).

The results of the TPD-MS measurements of HDT, PFDT, thiophenol, BM, benzeneselenol and BPT are presented in Figures S2-S7, respectively. Each of these figures includes a chemical structure of the investigated thiol, a mass spectrum of all species detected during the temperature ramp (averaged over the entire measurement), and intensity traces (ion current vs. temperature) for individual assigned ions. The high resolution of the mass analyzer allowed an exact assignment of molecular sum formulae to the detected ions. Maximum allowed deviation between the measured ion mass and the theoretical mass calculated based on the formula assignment was 5 ppm. In particular, in the case of HDT, the degree of unsaturation of every detected ion was determined from the elemental composition. The mass spectra presented in Figs. S2-S7 include contamination peaks (marked with asterisks), originating from plasticizers released from the teflon tubing at high temperatures.

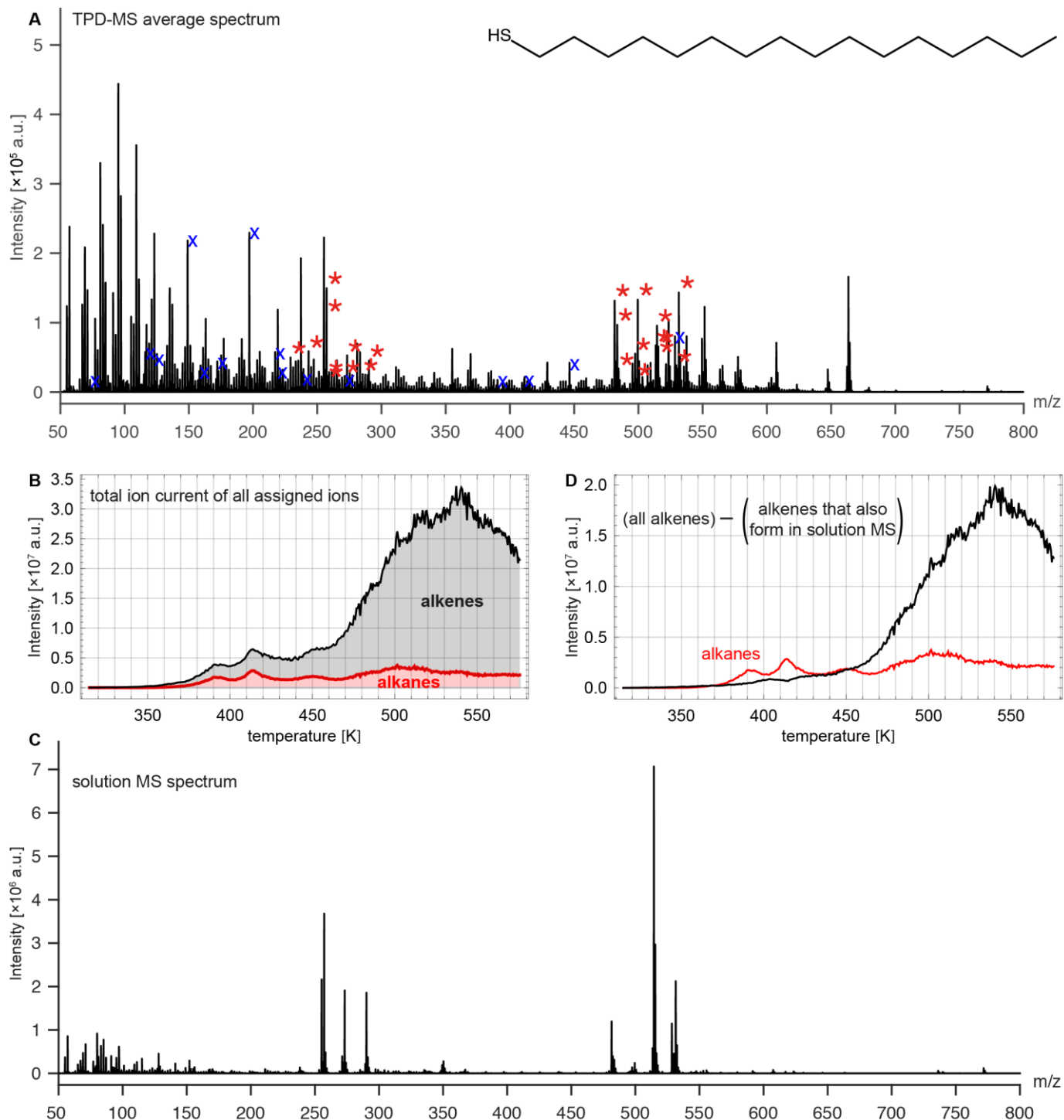


Figure S2. Ambient TPD-MS of a HDT SAM. (A) Mass spectrum of all ions desorbed from the sample, averaged from 296 to 573 K. Prominent peaks of species with saturated alkyl chains are marked with red asterisks. Contamination peaks and unassigned ions are marked with blue crosses. All other peaks represent species with unsaturated alkyl chains. (B) Total ion current of all assigned ions (with intensity > 20 000) plotted vs. sample temperature. Unsaturated species (gray fill) dominate over the saturated species (red fill). (C) Mass spectrum of a 16 mM solution of HDT in benzene, acquired using the same ionization method as the spectrum in Fig. A. Peaks of unsaturated species are also observed in the solution spectrum. This indicates that some of the

alkene chains observed in Figures A and B may form in the plasma ionization source. (D) Total ion current of the saturated (red) and unsaturated (black) species detected in TPD-MS, after subtraction of the alkene ions that were also detected in the solution MS experiment. Here, formation of unsaturated species occurs only above 450 K.

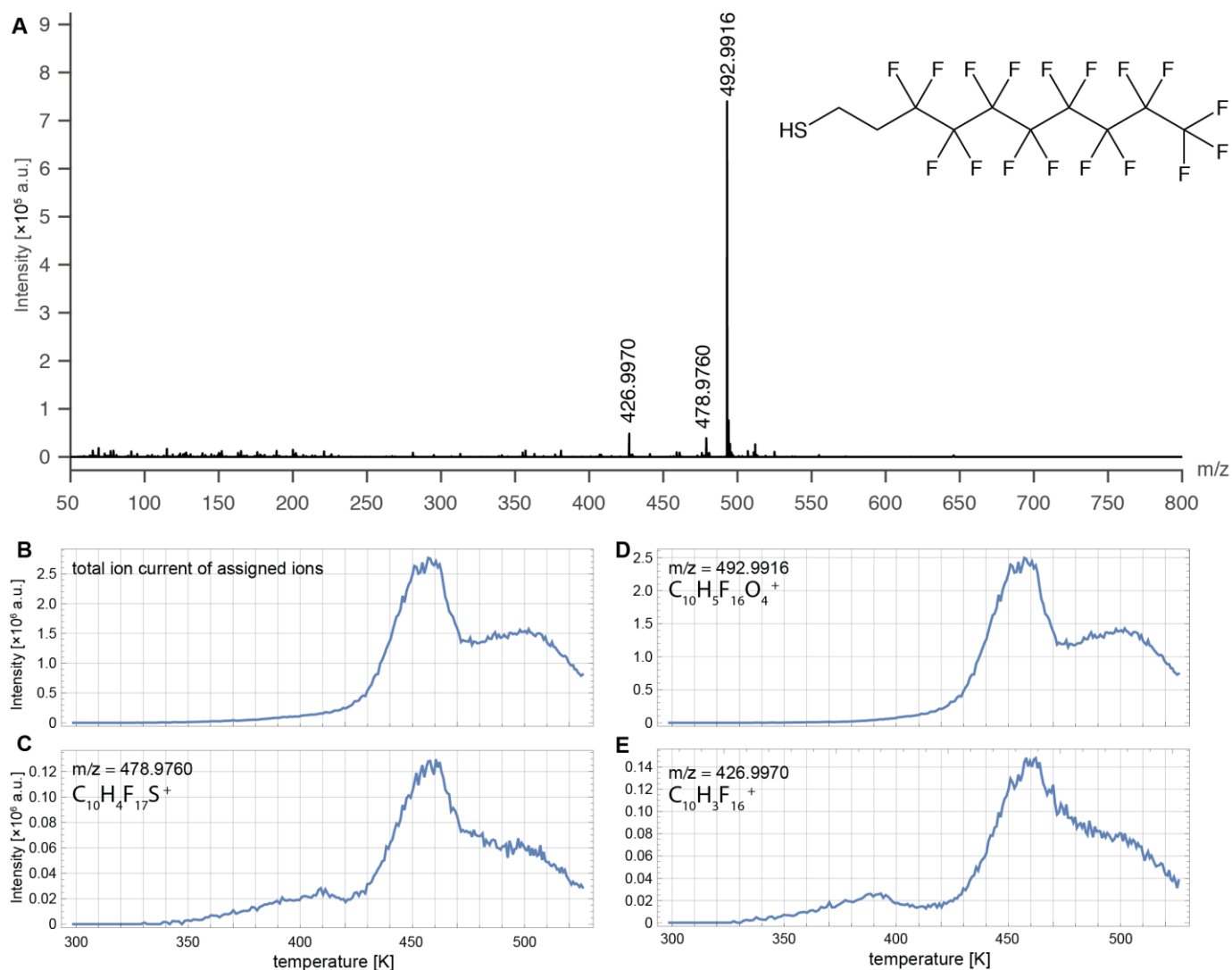


Figure S3. Ambient TPD-MS of a PFDT SAM. (A) The mass spectrum of all ions desorbed at temperatures from 296 to 523 K shows only species with 16 or 17 F atoms. Hence, massive abstraction of fluorine from PFDT was not observed upon heating the SAM. This means that the loss of fluorine observed in our TERS experiments (Fig. 2C) is not driven thermally, but by electronic transitions. (B) Total ion current of all ions originating from PFDT shows that desorption of PFDT from the Au surface occurs mostly above 420 K, which is above the temperature typically reached under the TERS tip (*cf.* Fig S8). Ion currents of the assigned ions are presented in Figures C-E.

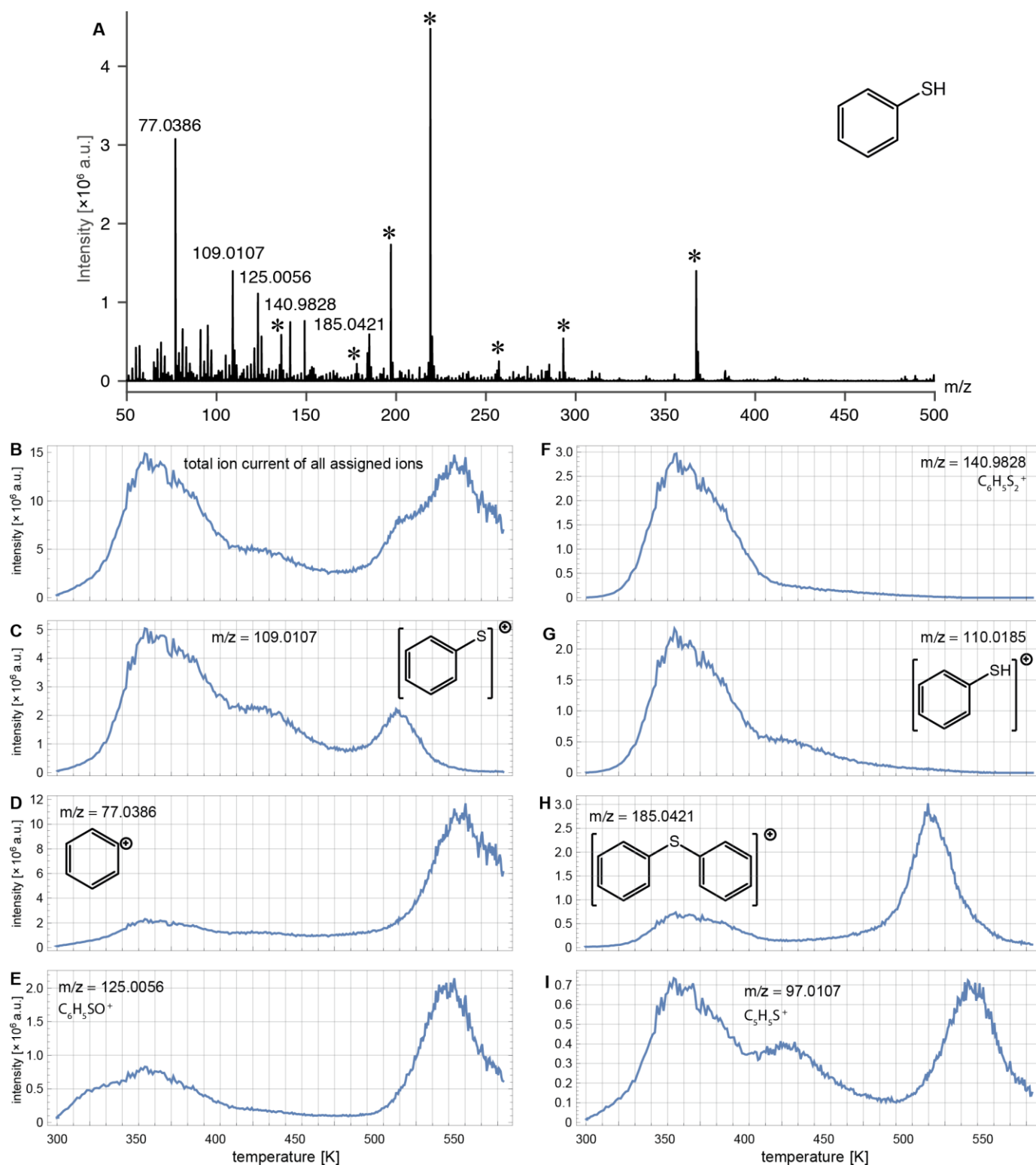


Figure S4. Ambient TPD-MS of a thiophenol SAM. (A) Mass spectrum of all ions desorbed from the sample, averaged from 296 to 573 K. Contamination peaks are marked with asterisks. (B) Total ion current of all assigned ions plotted vs. sample temperature. Thiophenol prepared from an ethanolic solution forms a SAM which is not very well ordered⁹, hence the differently arranged surface phases desorb at different temperatures, up to 573 K, which was the end of our measurement range. (C-I) TPD-MS traces for selected desorbed species, with their tentative structures.

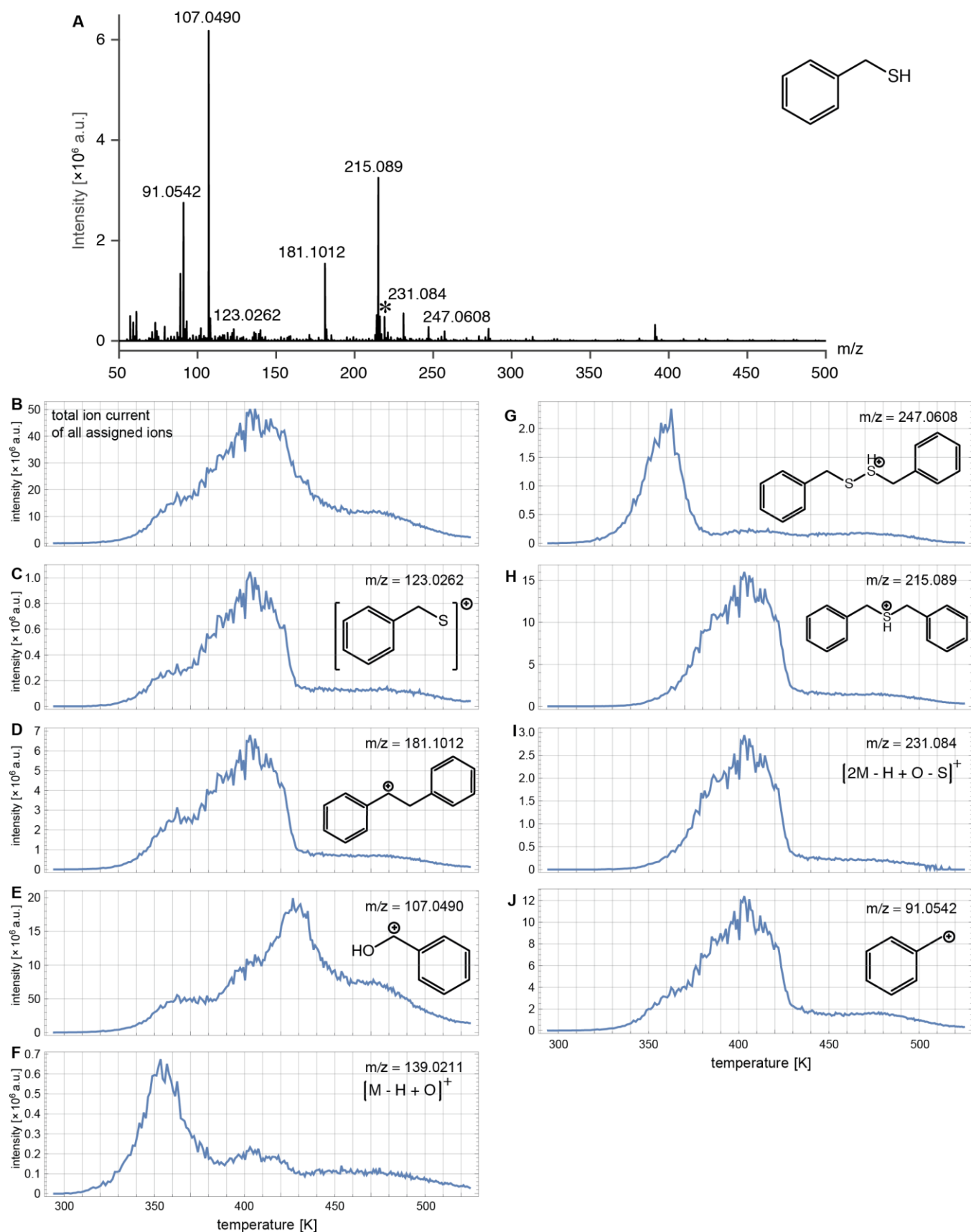


Figure S5. Ambient TPD-MS of a BM SAM. (A) Mass spectrum of all ions desorbed from the sample, averaged from 296 to 523 K. A contamination peak is marked with an asterisk. (B) Total ion current of all assigned ions plotted vs. sample temperature. (C-J) TPD-MS traces for selected desorbed species, with their tentative structures.

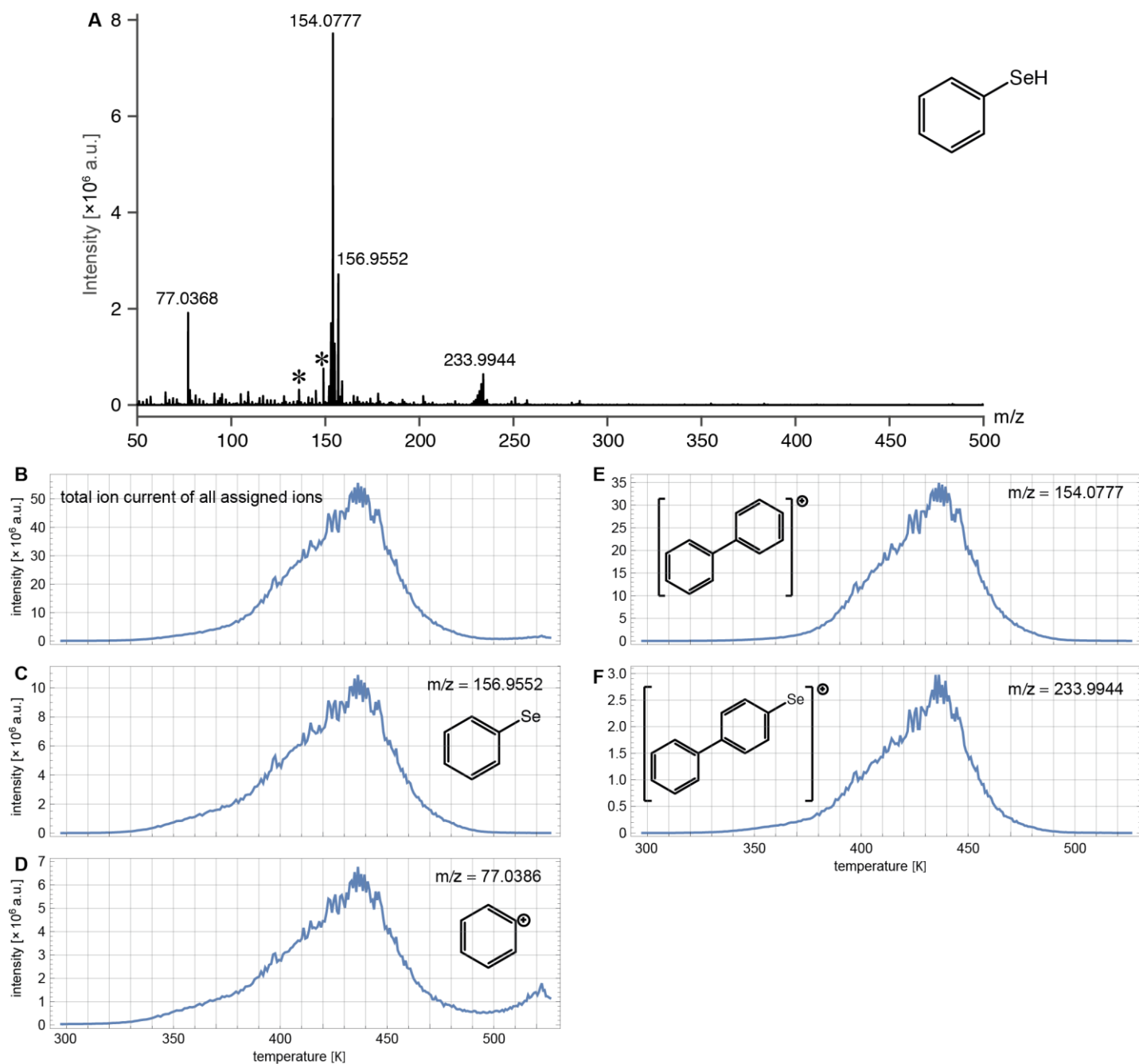


Figure S6. Ambient TPD-MS of a benzeneselenenol SAM. (A) Mass spectrum of all ions desorbed from the sample, averaged from 296 to 523 K. Contamination peaks are marked with asterisks. (B) Total ion current of all assigned ions plotted vs. sample temperature. (C-F) TPD-MS traces for selected desorbed species, with their tentative structures.

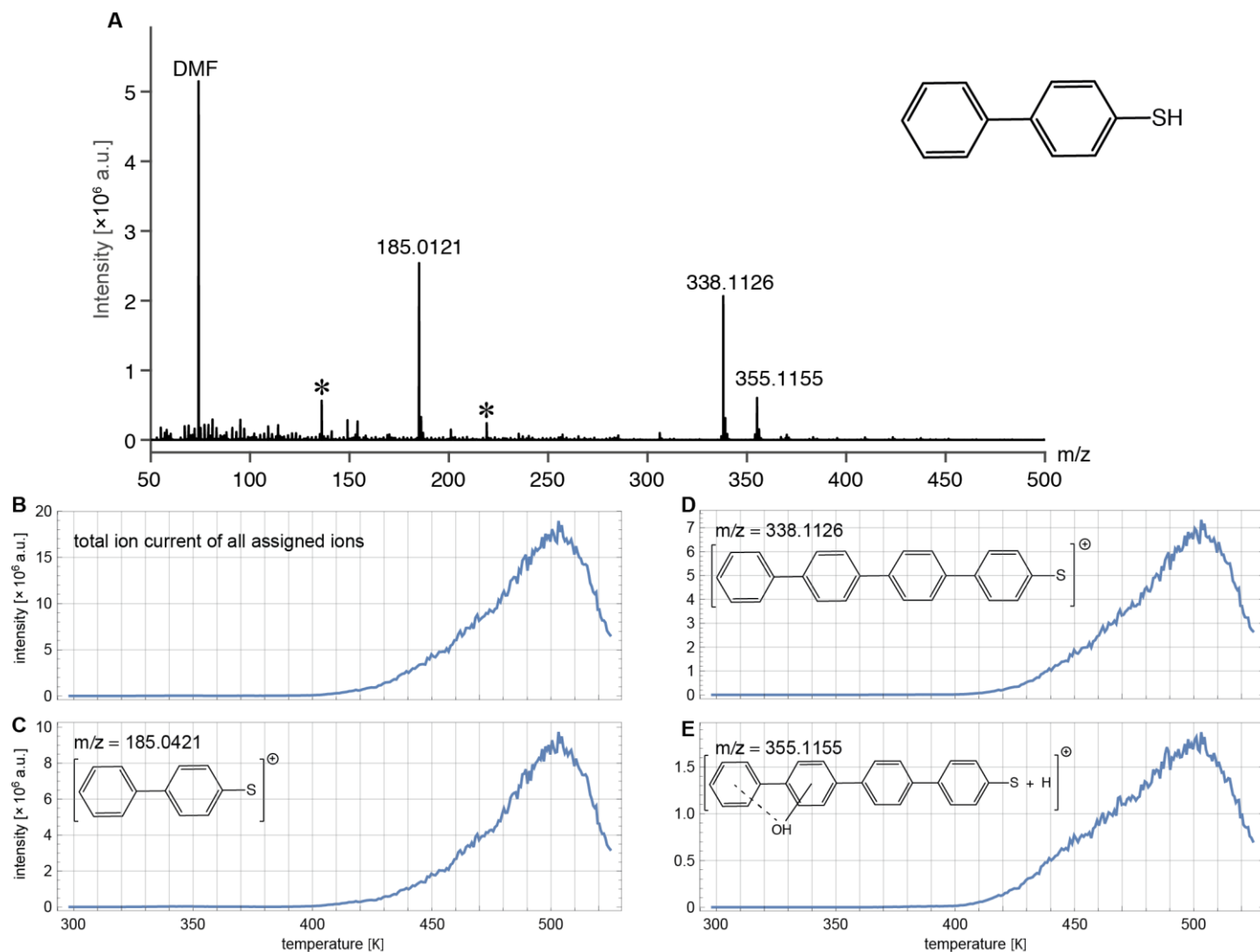


Figure S7. Ambient TPD-MS of a BPT SAM. (A) Mass spectrum of all ions desorbed from the sample, averaged from 296 to 523 K. Contamination peaks are marked with asterisks. (B) Total ion current of all assigned ions plotted vs. sample temperature. (C-E) TPD-MS traces for selected desorbed species, with their tentative structures.

S3. Measurement of the temperature in the hot spot

The temperature under the TERS tip (Fig. S8) was evaluated by fitting a Boltzmann distribution to the aS background¹⁰⁻¹². This approach was found to be the most reliable way of measuring the surface temperature of plasmonic nanostructures, unlike Stokes/anti-Stokes peak ratios, which are affected by wavelength-dependent prefactors and vibrational pumping¹³. We used the implementation

developed by Xie *et al.*¹², which relies on ratios of aS backgrounds, and cancels out the wavelength-dependent factors. The ratio of aS background intensities $I(\Delta\tilde{\nu})$ and $I_0(\Delta\tilde{\nu})$, measured at an unknown temperature T and at room temperature T_0 , respectively, is fitted with two Fermi-Dirac distributions:

$$\frac{I(\Delta\tilde{\nu})}{I_0(\Delta\tilde{\nu})} = \frac{\exp\left(-\frac{hc\Delta\tilde{\nu}}{kT_0}\right) - 1}{\exp\left(-\frac{hc\Delta\tilde{\nu}}{kT}\right) - 1},$$

where k is the Boltzmann constant. The fit is performed for the spectral region from -900 cm^{-1} to -300 cm^{-1} , excluding the TERS peaks.

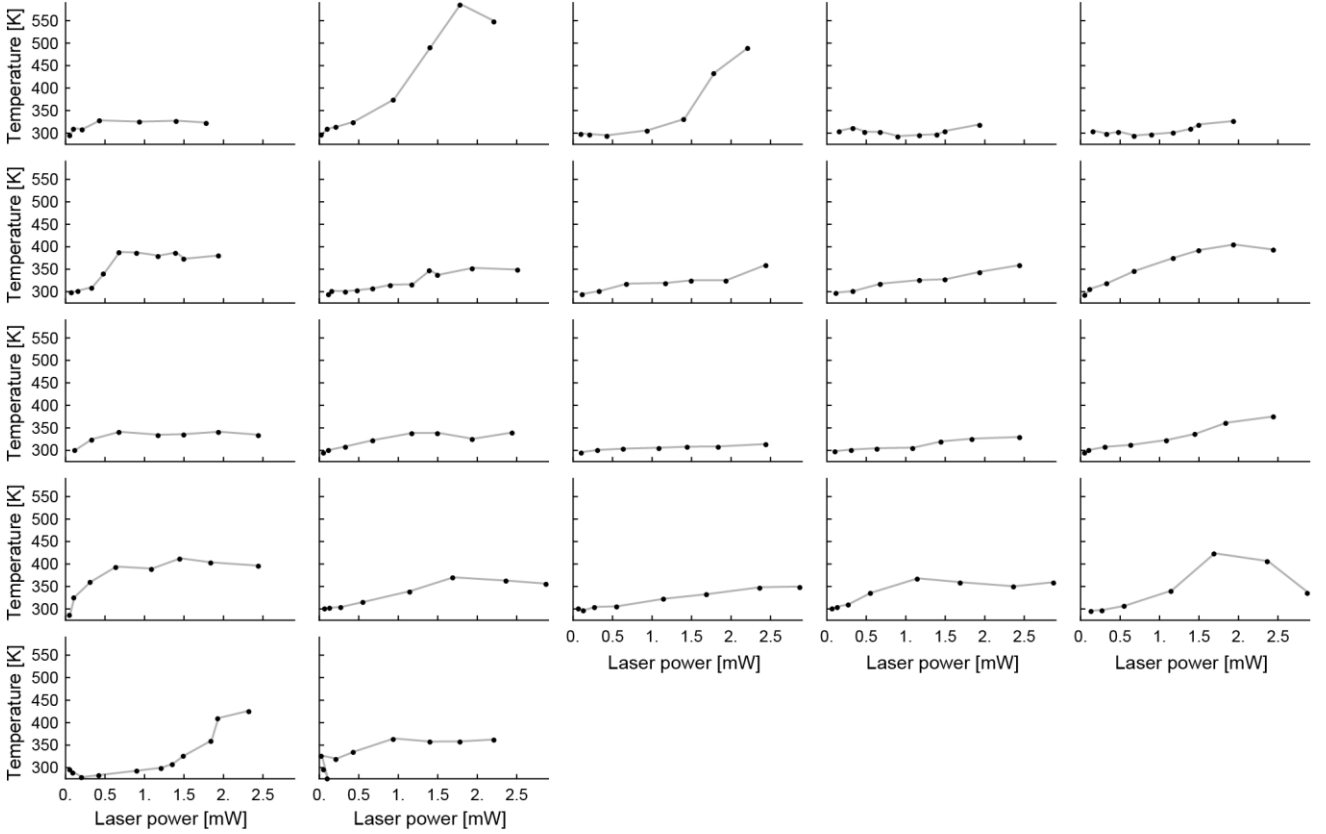


Figure S8. Temperature in the hot spot vs. incident laser power for 22 different TERS tips, extracted from the aS background of the TER spectra. The highest observed temperature was 587 K for a laser power of 1.79 mW, but for most tips the temperature did not exceed 420 K, even at the highest laser powers. Typical TERS experiments employ laser powers below 0.5 mW, which results in temperatures below 350 K.

The laser power employed in a typical TERS experiment does not exceed 0.5 mW.

Figures S8 shows that such low laser power results in temperatures below 350 K,

which are not high enough to induce pyrolysis or autoignition of organic molecules. Yet, they may be sufficiently high to desorb the sample.

For many tips, the relation between the laser power and the hot spot temperature was found to be nonlinear. This observation contradicts a frequent assumption in photocatalysis research, namely that the surface temperature of a plasmonic substrate depends linearly on the intensity of the incident light. This assumption implies that reactions driven by plasmonic heating are governed by Arrhenius kinetics, with an exponential dependence of the reaction rate on the laser power. This indirect kinetic argument is used by catalysis research to discriminate between thermally driven and charge-induced reactions. Figure S8 demonstrates directly that this argument is not valid at the level of a single hot spot.

We presume that the nonlinearity of the temperature vs. laser power relation is caused by a change in morphology of the hot spot at an elevated temperature, which leads to a change in the electromagnetic enhancement and in the rate of plasmonic heating.

S4. Fermi-Dirac vs. Boltzmann distribution

We use the Boltzmann distribution to describe the energies of the electrons in Figures 3, S10 and S18, instead of the quotient of the Fermi-Dirac distributions used in Fig. S8. Below we outline the reasons for this approximation and prove its validity.

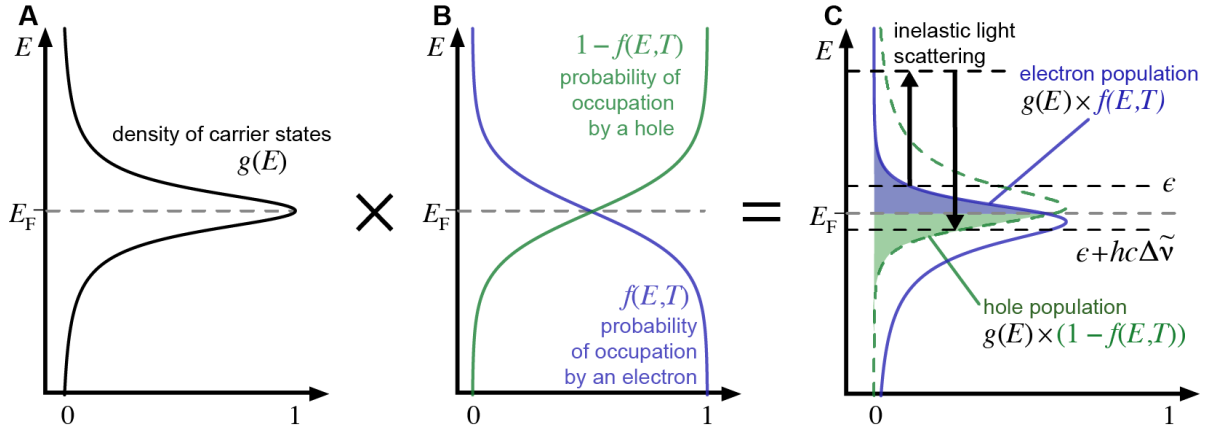


Figure S9. Inelastic light scattering off electrons in the metal gives rise to Boltzmann-distributed aS background. Density of states of the surface carriers in a metallic nanostructure (A), multiplied by the Fermi-Dirac probability of occupation by an electron/hole (blue/green line in B), gives the populations of electrons (blue line in C) and holes (dashed green line in C). Incident laser photons are inelastically scattered (black arrows in C) by excitation of electrons from states above the Fermi energy E_F (blue fill in C) into unoccupied states below E_F (green fill in C). The populations of these electrons and hole can be approximated with Boltzmann distributions. The intensity of the transition is determined by the product of the two Boltzmann-distributed populations, hence it is also Boltzmann-distributed and forms an exponentially decaying background.

The aS background arises from inelastic light scattering off electrons in the plasmonic metal (Figure S9). The intensity of the background $I(\Delta\tilde{\nu})$ is related with the density of states of the surface electrons $g(E)$ and the Fermi-Dirac probability of occupation $f(E,T)$, according to the formula proposed by Otto *et al.*¹⁰:

$$I(\Delta\tilde{\nu}) = \int g(\epsilon)f(\epsilon)g(\epsilon + hc\Delta\tilde{\nu})(1 - f(\epsilon + hc\Delta\tilde{\nu})) d\epsilon .$$

This formula is strict, yet not practical – it requires assuming an analytical expression for $g(\epsilon)$ and fitting an integral to the aS background. Hence, Hugall *et al.* proposed to approximate $f(\epsilon)$ with a Boltzmann distribution¹¹. Strictly, the electron occupation $f(\epsilon)$ is approximated with $\exp(-(\epsilon - E_F)/kT)$, where E_F is the Fermi energy of the plasmonic metal. The hole occupation $1 - f(\epsilon + hc\Delta\tilde{\nu})$ is

approximated with $\exp((\epsilon + hc\Delta\tilde{\nu} - E_F)/kT)$, which simplifies the expression for $I(\Delta\tilde{\nu})$ to:

$$\begin{aligned} I(\Delta\tilde{\nu}) &= \int g(\epsilon)g(\epsilon + hc\Delta\tilde{\nu}) \exp(hc\Delta\tilde{\nu}/kT) d\epsilon = \\ &= \exp(hc\Delta\tilde{\nu}/kT) \times \int g(\epsilon)g(\epsilon + hc\Delta\tilde{\nu}) d\epsilon . \end{aligned}$$

The aS background intensity $I(\Delta\tilde{\nu})$ is dominated by the exponential factor $\exp(hc\Delta\tilde{\nu}/kT)$, because the integral $\int g(\epsilon)g(\epsilon + hc\Delta\tilde{\nu}) d\epsilon$ changes slowly for small $\Delta\tilde{\nu}$. The exponential term dominates for Raman shifts $\Delta\tilde{\nu}$ smaller than the width of $g(\epsilon)$, which is the case in our experiment. The validity of this assumption is supported by the values of $g(\epsilon)$ half-widths reported previously^{11,14}, as well as by the excellent match between the Boltzmann model and the aS backgrounds measured in SERS and TERS (Figures 3, S10, S18). The deviation between the Fermi-Dirac and the Boltzmann distribution becomes significant only for Raman shifts between -300 and 0 cm^{-1} , which lie out of our measurement range.

The aS background in the SER spectrum of BM acquired at 2.38 mW (Fig. 3E) was fitted with a two-temperature model, *i. e.* a sum of two Boltzmann distributions (Fig. S10). The fitted function was:

$$\log I(\Delta\tilde{\nu}) = \log \left(A_1 \exp \left(\frac{hc\Delta\tilde{\nu}}{kT_1} \right) + A_2 \exp \left(\frac{hc\Delta\tilde{\nu}}{kT_2} \right) \right)$$

for $\Delta\tilde{\nu}$ between -3699 cm^{-1} (the smallest wavenumber for which the aS background exceeds $3 \times \text{CCD noise}$) and -317 cm^{-1} (notch filter cutoff). Fitting the function to the logarithm of the aS background $\log I(\Delta\tilde{\nu})$, instead of the aS background itself, allowed an exact match of the fitted function to both the thermal part of the spectrum (blue line, effective temperature T_1) and to the hot-carrier tail (dashed gray line, effective temperature T_2).

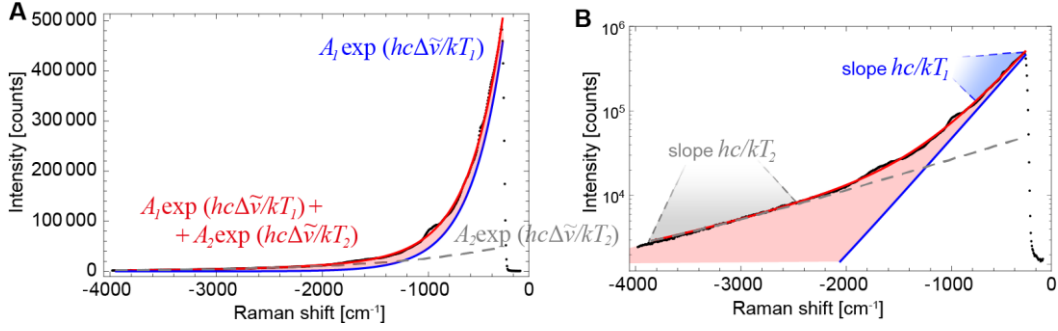


Figure S10. Two-temperature model fit to the aS background plotted on a linear scale (A) and on a semilogarithmic scale (B). The contribution of the hot electrons is marked with a light red fill.

The fitted coefficients were $A_1 = (1.22 \pm 0.02) \times 10^6$ counts, $T_1 = 440 \pm 4$ K, $A_2 = (63 \pm 2) \times 10^3$ counts and $T_2 = 1630 \pm 30$ K. The resulting share of hot electrons in the total electron population was:

$$\frac{\int_{-\infty}^0 A_2 \exp\left(\frac{hc\Delta\tilde{\nu}}{kT_2}\right) d(\Delta\tilde{\nu})}{\int_{-\infty}^0 A_1 \exp\left(\frac{hc\Delta\tilde{\nu}}{kT_1}\right) + A_2 \exp\left(\frac{hc\Delta\tilde{\nu}}{kT_2}\right) d(\Delta\tilde{\nu})} = \frac{\frac{A_1 k T_1}{hc}}{\frac{A_1 k T_1}{hc} + \frac{A_2 k T_2}{hc}} = \frac{A_1 T_1}{A_1 T_1 + A_2 T_2} = 16.1 \pm 0.5 \, \%.$$

However, this value is subject to gross errors: (i) the wavelength-dependent factors that were eliminated in TERS thermometry (instrument throughput, plasmon resonance profile, see Section S3), are not compensated in the present analysis, (ii) the fit function is oversimplified (missing mixed terms in the integral $I(\Delta\tilde{\nu})$ for two temperatures). Hence, more rigorous analysis is required to quantify the energy distribution of hot electrons, and to verify how exactly it follows Boltzmann statistics.

S5. Identification of fluctuations in SER spectra

Results shown in Fig. 5 were extracted from 4096 SER spectra of thiophenol, 6400 spectra of BM, 4864 spectra of benzeneselenol and 2304 spectra of BPT. We employed a machine learning algorithm¹⁵ for identifying the fluctuating spectra within the data sets for thiophenol, BM and benzeneselenol. The spectra of BPT

included too few fluctuations to train the algorithm, so they were categorized manually. Every data point consisted of a normalized fragment of the SER spectrum between 362 and 1893 cm^{-1} (351 pixels on the CCD). We then used a support vector classification (SVC) to assign the SER spectra into one of three classes: clean spectra of the SAM, spectra with fluctuations, or spectra with no signal from the SAM (Figure S11). The training sets consisted of 481 spectra for thiophenol, 714 spectra for BM and 505 spectra for benzeneselenol. The test sets consisted of 300 spectra for each thiol. All training and test sets were randomly chosen from the complete data sets, hence the abundance of clean spectra, spectra with fluctuations and spectra with no signal in the selected sets was representative for the complete data sets.

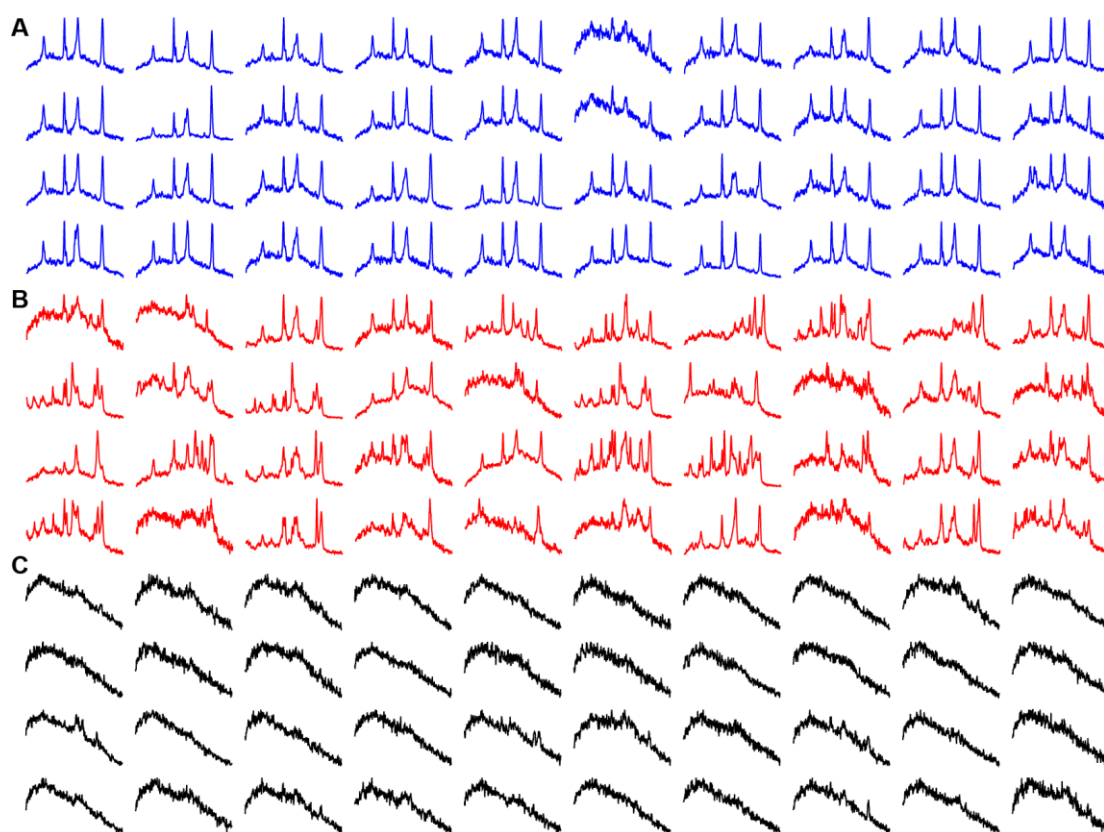


Figure S11. SER spectra of a BM SAM were classified into three categories: (A) clean spectra of the BM SAM, (B) spectra with fluctuations due to carbonaceous species and (C) spectra with no signal from the BM SAM (after desorption).

Multi-class C -SVC was executed for classification of the spectra using the “one-on-one” approach. For every pair of classes i, j and a training set $\{x_t\}$ the following optimization problem was solved:

$$\min_{w^{ij}, b^{ij}, \xi^{ij}} \frac{1}{2} (w^{ij})^T w^{ij} + C \sum_t (\xi^{ij})_t$$

with constraints:

$$(w^{ij})^T \phi(x_t) + b^{ij} \geq 1 - \xi_t^{ij}, \text{ if } x_t \text{ is in the } i\text{-th class,}$$

$$(w^{ij})^T \phi(x_t) + b^{ij} \leq -1 + \xi_t^{ij}, \text{ if } x_t \text{ is in the } j\text{-th class,}$$

$$\xi_t^{ij} \geq 0.$$

Weights $\{w^{ij}\}$, bias $\{b^{ij}\}$ and slack variables $\{\xi^{ij}\}$ were optimized using a radial basis function kernel:

$$K(x_i, x_j) = \phi(x_i)^T \phi(x_j) = \exp(-\gamma \|x_i - x_j\|^2).$$

The slack variables were computed using a hinge loss function. Details of the sequential minimal optimization algorithm are described in the LIBSVM implementation documentation¹⁶.

The regularization parameter C and the kernel parameter γ were tuned using a grid search. We picked $C = 100$ and γ equal to 0.007, 0.003 and 0.005 for thiophenol, BM and benzeneselenol, respectively. Classification scores for all training sets and test sets are summarized in Table S1. Average precision and recall scores were above 0.95 for thiophenol, and above 0.99 for BM and benzeneselenol. The main goal of this analysis was to detect the spectra with fluctuations within the data sets (Figure S12). Hence, recall scores for the spectra with fluctuations was the key measure of the quality of the classification. These

recall values were above 0.8 for all test sets, which allowed efficient detection of the fluctuations in the complete data sets.

Table S1. SVC scores show satisfactory recall (>0.8) of carbonaceous fluctuations in the test sets for all SAMs. The high number of support vectors for thiophenol indicates difficulties in classification of the spectra (see Fig. S15).

		thiophenol	BM	Benzeneselenol
training set	recall of fluctuating spectra	67/70 = 0.96	34/37 = 0.92	25/30 = 0.83
	number of data points	481	714	505
	number of support vectors	198	100	115
test set	recall of fluctuating spectra	26/32 = 0.81	8/9 = 0.89	7/8 = 0.88

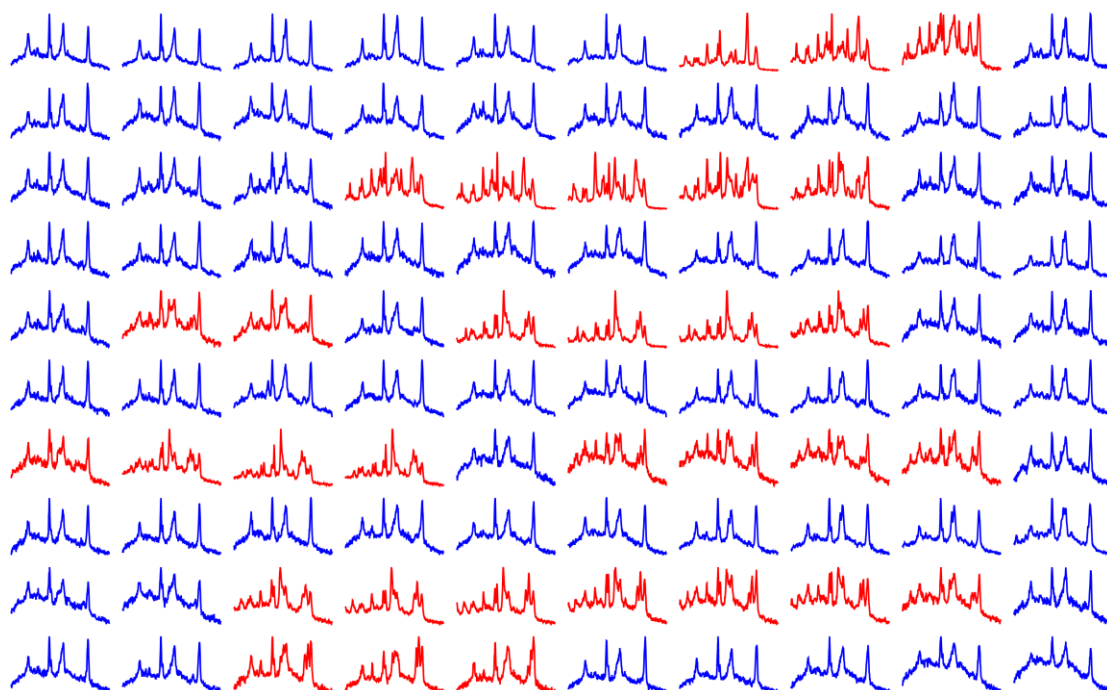


Figure S12. Classification of the SER spectra of BM measured at a sample temperature of **376 K**. Clean spectra are marked in blue, whereas spectra with fluctuations are marked in red. The rate of fluctuations is very high, due to intense desorption of BM at 376 K.

Consistency of the classification is demonstrated in Figures S13 and S14. The histograms in Fig. S13 show the number of spectra assigned to the three classes for thiophenol, BM and benzeneselenol. For every sample, the number of clean spectra decreases with increasing sample temperature (blue bars), due to sample desorption. Concurrently, the number of spectra with no signal from the SAM increases (black bars), along with gradual desorption. Spectra with fluctuations (red bars) are most frequent at the temperatures where sample desorption starts. Figure S14 shows the average of all clean spectra of BM (A), of all spectra with fluctuations (B), and of all spectra with no SAM signal. Spectrum A shows only the peaks of BM, which agrees with the expectations for clean spectra. Spectrum B shows the same peaks, lying on top of two broad background humps. This broad background emerges due to averaging of the fluctuations and resembles the spectrum of amorphous carbon, similar to Fig. 4. Spectrum C shows no peaks of BM, which confirms complete desorption of the sample. Overall, the average spectra prove the validity of the classification.

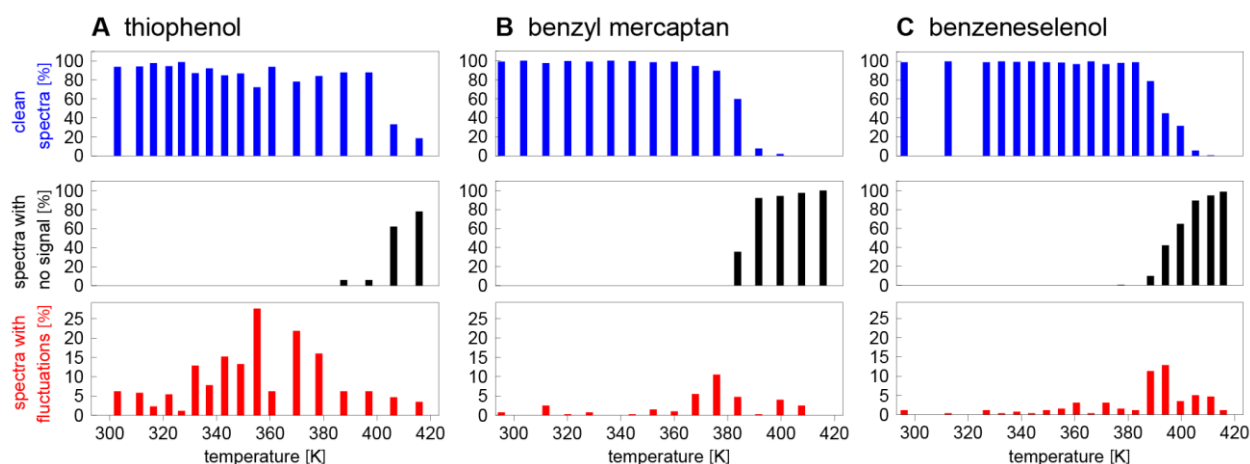


Figure S13. Classification of the SER spectra of thiophenol (A), BM (B) and benzeneselenol (C) – analysis of complete SERS data sets. Blue bars represent the number of clean spectra of the SAM for a given temperature. That number decreases with progressing sample desorption. Black bars represent the number of spectra with no signal of the SAM. That number increases with sample desorption. Red bars represent the number of spectra with fluctuating bands. Appearance of the fluctuations coincides with the onset of sample desorption.

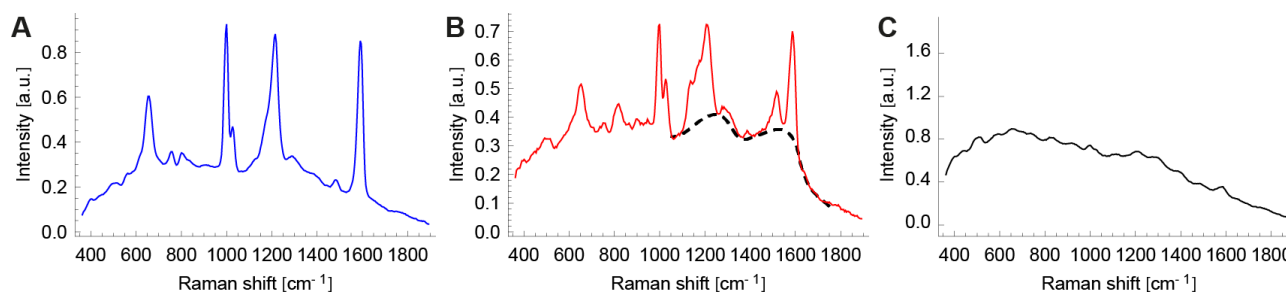


Figure S14. Average of the three classes of spectra for BM. (A) Average of all clean SER spectra of BM. (B) Average of all SER spectra of BM showing carbonaceous fluctuations. The fluctuations average out to two broad background humps, similar to Fig. 4. (C) Average of all SER spectra of BM showing no signal from the SAM.

The classification was ambiguous for the SER spectra of thiophenol acquired at high temperatures (≥ 406 K). As shown in the TPD-MS trace of thiophenol in Fig. 5A, this SAM does not desorb completely up to 520 K. Hence, a significant number of the spectra show a residual signal of the molecules of thiophenol remaining on the surface. These peaks have a very low signal/noise ratio, hence differentiation between clean spectra of thiophenol and spectra with no signal becomes difficult. An example of such ambiguous classification of weak spectra is presented in Figure S15. The spectra with residual signal of thiophenol can be categorized as clean, if they do not include any fluctuating features. Yet, they could also be categorized as “no signal”, if the peaks hardly emerge out of the noise. Hence, the ambiguity in the classification of weak spectra is an inherent feature of this kind of spectra. It reflects the way how the algorithm was trained, and is not introduced by the algorithm itself. The ambiguity of this case is further demonstrated by the high number of support vectors identified by SVC for the SER spectra of thiophenol (Table S1).

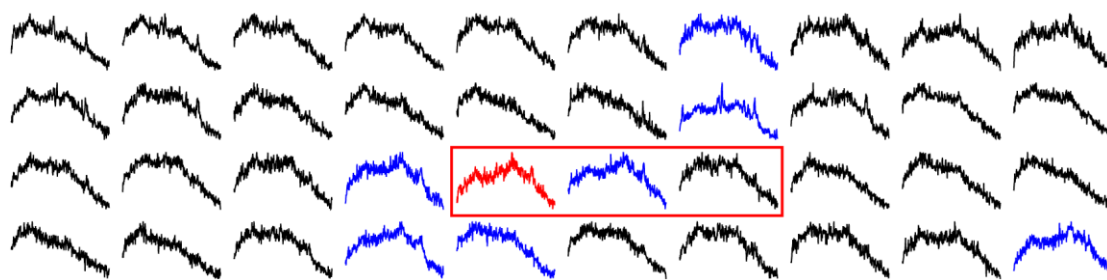


Figure S15. Ambiguous classification of the SER spectra of thiophenol measured at a sample temperature of 416 K. The three spectra marked with a rectangle look very similar. Yet, SVC classified them into three different categories.

Further Supporting Figures

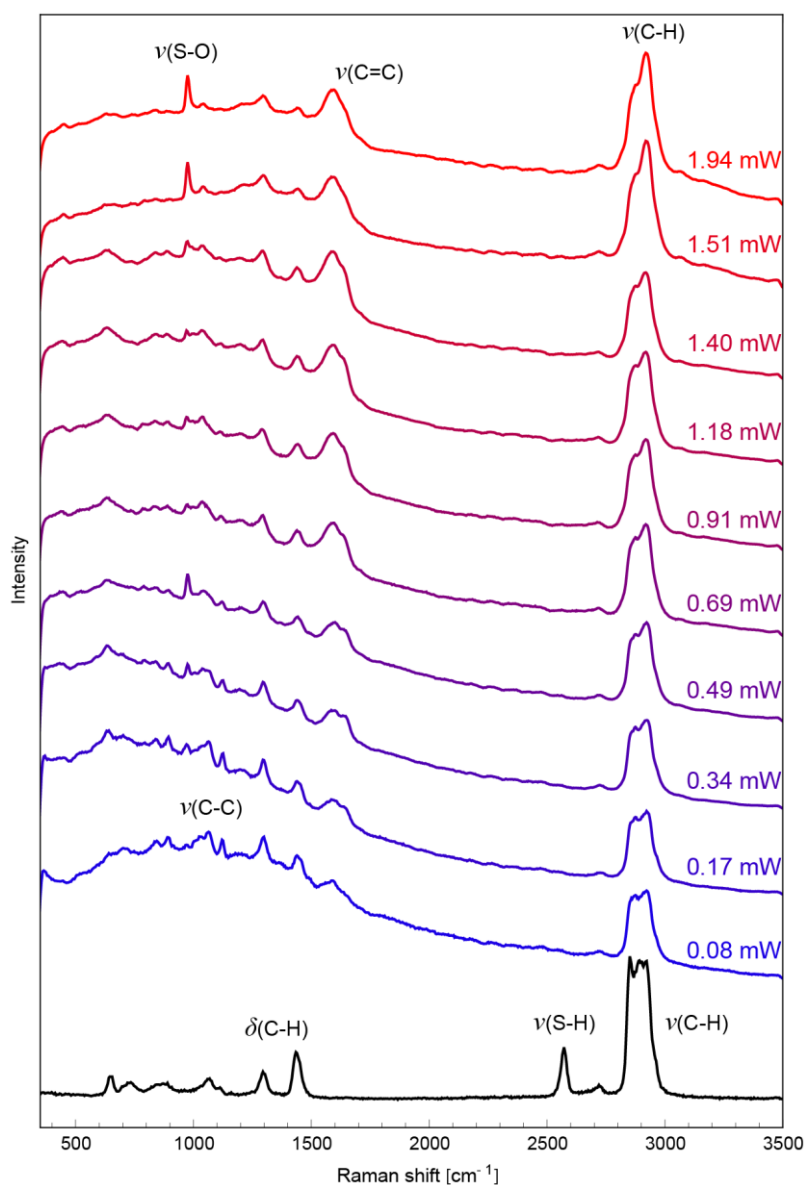


Figure S16. Tip-induced reactions in a decanethiol SAM as a function of laser power.

Confocal Raman spectrum marked in black. The spectral changes are similar to the ones observed in HDT SAM (Fig. 2A).

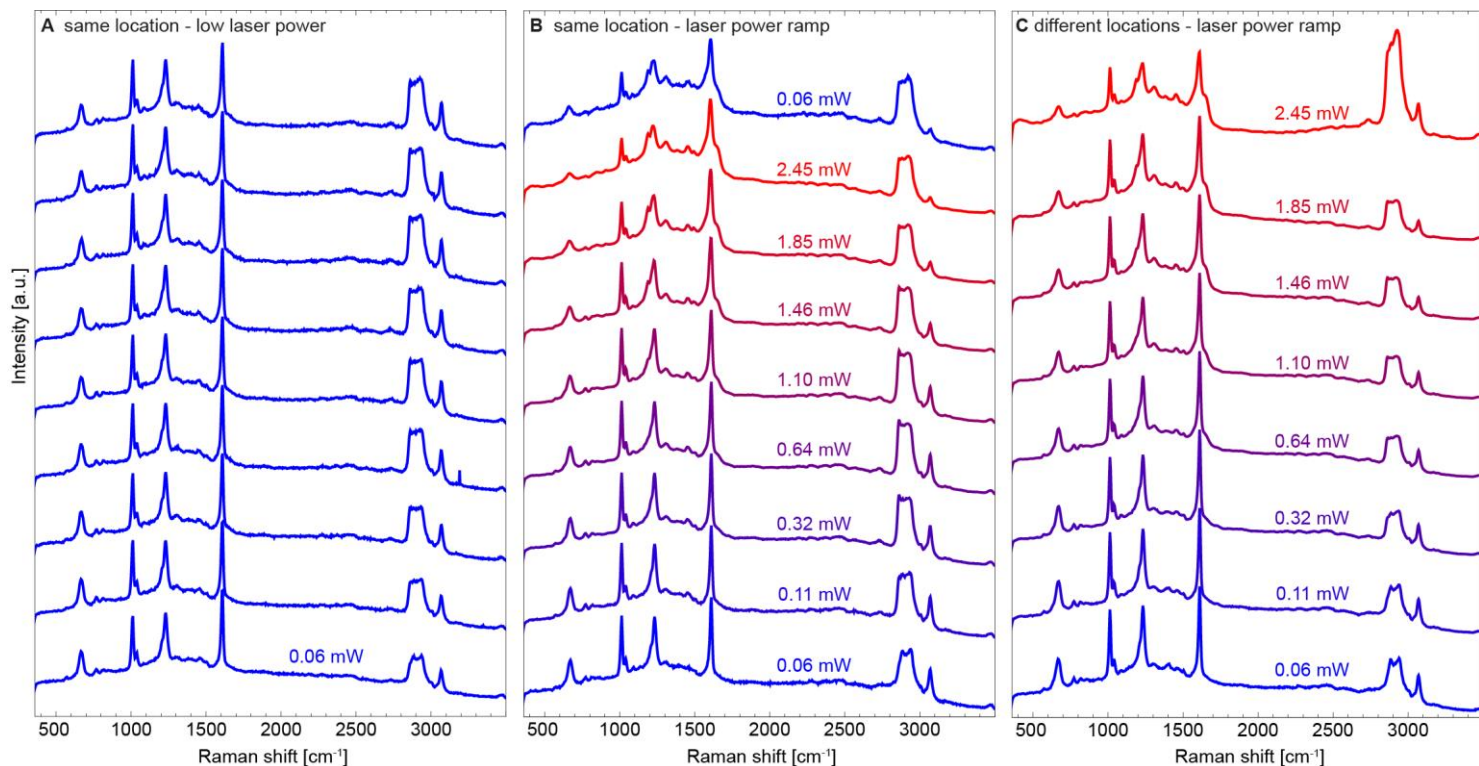


Figure S17. Effect of irradiation time and total energy dose on the progress of crosslinking

in a BM SAM. (A) Acquisition of a series of TERS spectra over the same $1\ \mu\text{m} \times 1\ \mu\text{m}$ region of a BM SAM location at a low laser power (0.058 mW) does not induce crosslinking in the monolayer. (B) Acquisition of TERS spectra under similar conditions, but with increasing laser power, leads to gradual crosslinking of the monolayer, similar to the one presented in Fig. 3C. (C) Acquisition of TERS spectra at increasing laser power, over a different sample region for every acquisition, yields a similar result as the one shown in Fig. B. Hence, the progress of the plasmon-induced reactions is mostly a function of the incident laser power. The total time the sample stays under the tip is of secondary importance.

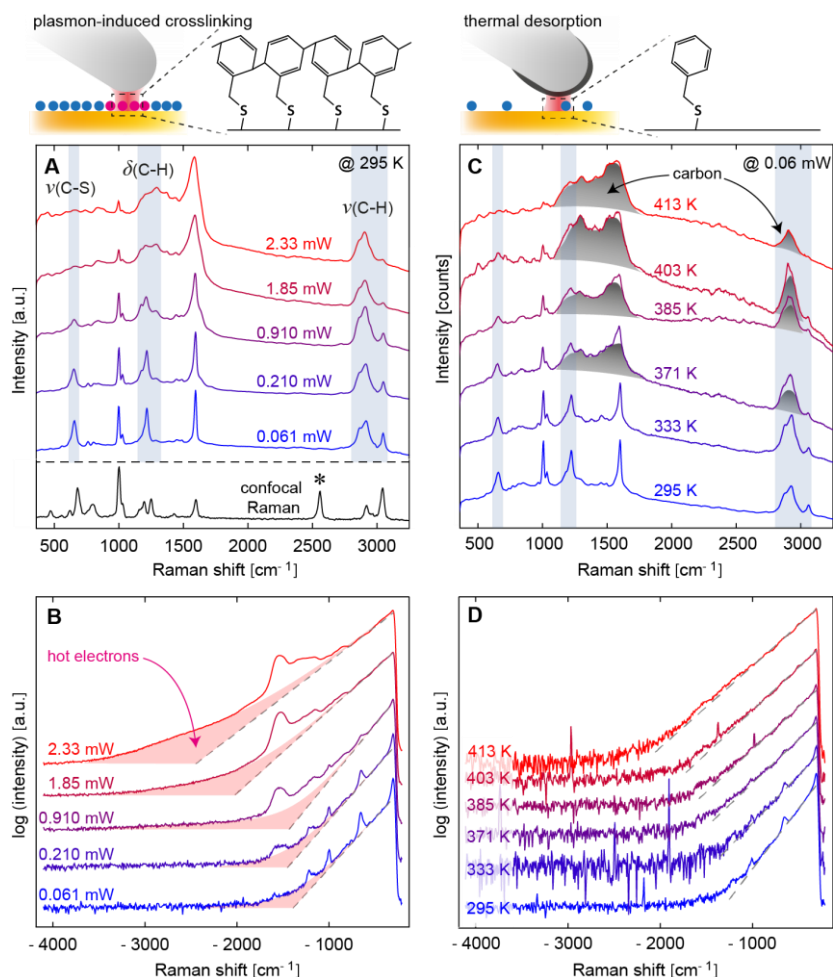


Figure S18. TERS spectra of a BM SAM acquired at different laser powers and sample temperatures, analogous to the SER spectra shown in Fig. 3 in the main text. The spectra presented were acquired over $1\ \mu\text{m} \times 1\ \mu\text{m}$ regions of a BM SAM adsorbed on a flat Au substrate. (A) Crosslinking in a BM SAM as a function of the laser power. The spectral changes are similar to the ones in SERS (Fig. 3A) and to the ones in Fig. S17B&C and S22, however the reaction progresses further than in Fig. 3A – the SAM finally turns into a disordered layer of hydrocarbons, showing broad spectral features at 2.33 mW. (B) Appearance of the hot-electron Boltzmann component in the aS background at high laser powers is consistent with the observations from SERS (Fig. 3E). (C) TERS temperature ramp on a BM SAM, from 295 to 413 K. The Stokes spectral features are the same as for temperature-ramped SERS (Fig. 3D), except for additional broad bands at 1250, 1550 and $2900\ \text{cm}^{-1}$ corresponding to carbon deposits on the tip (marked with dark grey fill). (D) The aS background follows the Boltzmann exponential decay, similar to the TERS spectra shown in Fig. 3F. All spectra in Figs. A-D are offset for better visibility, but not scaled.

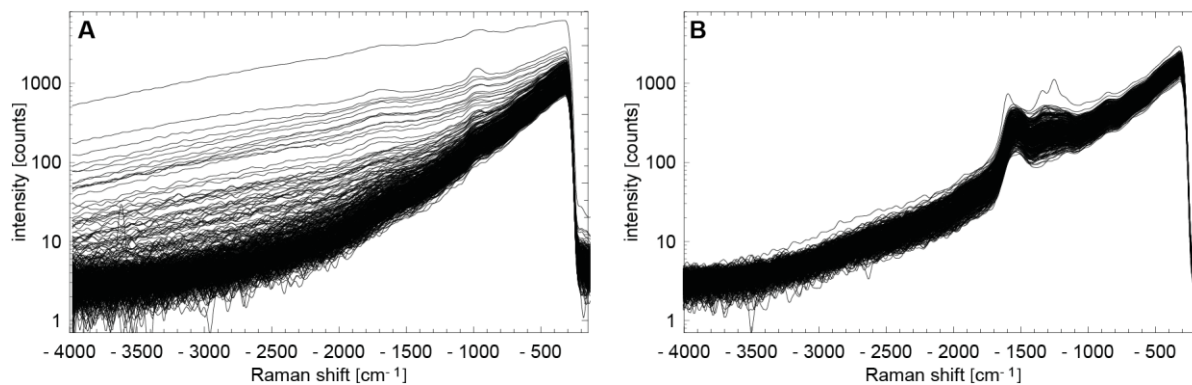


Figure S19. AS background for a single hot spot vs. multiple hot spots. (A) AS backgrounds of a BM SAM recorded at 400 locations on a SERS substrate – these spectra add up to the 2.37 mW SER spectrum presented in Fig. 3E. (B) AS backgrounds recorded with a TERS tip scanned over 400 locations on a flat sample of BM SAM – these spectra add up to the 2.33 mW TER spectrum presented in Fig. S18B. TERS yields a very reproducible aS background, whereas the background recorded on the SERS substrate varies greatly with location. The aS background is similar for most of the presented SER spectra, but it is markedly higher for a small number of spectra, which were acquired at hot spots with extraordinarily high electromagnetic enhancement. The variability in the aS background arises from the inhomogeneity of enhancement over the substrate surface¹⁷, and leads to a variability of the reaction products. Consequently, the spectral patterns of the reaction products in SERS (Fig. 3C) are not as clear as in TERS (Fig. S17B,C, S18, S22), due to averaging over many hot spots with different enhancements and surface geometries.

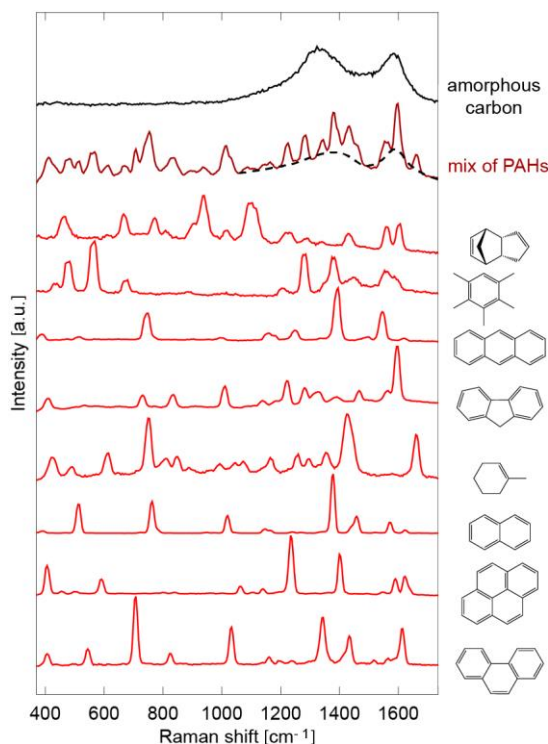


Figure S20. The fluctuating bands in SERS and TERS resemble the Raman spectra of mixed random PAHs. The Raman spectra of selected polycyclic species (dicyclopentadiene, pentamethylbenzene, anthracene, fluorene, 1-methyl-1-cyclohexene, naphthalene, pyrene, phenanthrene, plotted in red) include bands around 1350 and 1600 cm^{-1} , which correspond to C-H bending and C-C stretching within the aromatic rings. However, these peaks appear at slightly different positions for different PAHs, due to the differences in molecular geometry. Averaging the spectra of the PAHs results in a spectrum with many sharp peaks (plotted in dark red), and two small background humps around 1350 and 1600 cm^{-1} (dashed black line), resembling the spectrum of amorphous carbon (plotted in black). Remarkably, sample degradation in TERS also manifests itself with intense fluctuating bands around 1350 and 1600 cm^{-1} , which average out to two broad humps (*cf.* Fig. 4). Hence, we hypothesize that the fluctuating bands in TERS result from a mix of polycyclic intermediates and similar organic compounds with a range of molecular geometries that eventually turn into amorphous carbon on the tip.

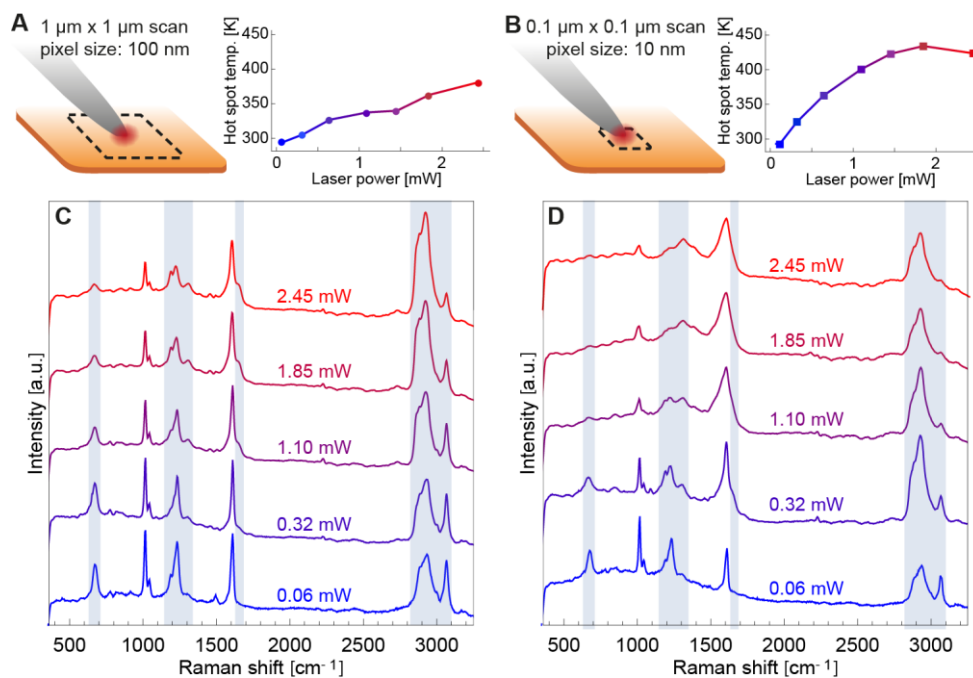


Figure S22. Interplay between plasmon-induced reactions and plasmonic heating.

Plasmonic heating of the TERS hot spot is more efficient for small sample scans than for large scans, due to the poorer heat dissipation and the prolonged residence of the tip over a small sample region. The different rates of heat accumulation are reflected by the gentle increase in the temperature upon ramping the laser power for $1\ \mu\text{m} \times 1\ \mu\text{m}$ scans (A), and the steep increase in the temperature for $0.1\ \mu\text{m} \times 0.1\ \mu\text{m}$ scans (B). Plasmon-driven crosslinking in a BM SAM is also more efficient for small scan sizes ($0.1\ \mu\text{m} \times 0.1\ \mu\text{m}$, Fig. D) than for large scan sizes ($1\ \mu\text{m} \times 1\ \mu\text{m}$, Fig. C). This observation can be explained by an increase in the DEA cross-sections with temperature, due to the higher occupation of vibrationally excited levels¹⁸. A similar effect was postulated by Christopher *et al.* in the context of photocatalytic hydrocarbon conversion¹⁹. The synergy between plasmon-driven reactions and plasmonic heating is of critical for the control of plasmon-induced photocatalytic reactions. All spectra presented were acquired on the same sample using the same tip.

References

- (1) Paulite, M.; Blum, C.; Schmid, T.; Opilik, L.; Eyer, K.; Walker, G. C.; Zenobi, R. *ACS Nano* **2013**, *7*, 911–920.
- (2) Opilik, L.; Payamyar, P.; Szczerbiński, J.; Schütz, A. P.; Servalli, M.; Hungerland, T.; Schlüter, A. D.; Zenobi, R. *ACS Nano* **2015**, *9*, 4252–4259.
- (3) Zhang, W.; Yeo, B. S.; Schmid, T.; Zenobi, R. *J. Phys. Chem. C* **2007**, *111*, 1733–1738.
- (4) Weiss, E. A.; Kaufman, G. K.; Kriebel, J. K.; Li, Z.; Schalek, R.; Whitesides, G. M. *Langmuir* **2007**, *23*, 9686–9694.
- (5) Stadler, J.; Schmid, T.; Opilik, L.; Kuhn, P.; Dittrich, P. S.; Zenobi, R. *Beilstein J. Nanotechnol.* **2011**, *2*, 509–515.
- (6) Nudnova, M. M.; Zhu, L.; Zenobi, R. *Rapid Commun. Mass Spectrom.* **2012**, *26*, 1447–1452.
- (7) Wolf, J. C.; Schaer, M.; Siegenthaler, P.; Zenobi, R. *Anal. Chem.* **2015**, *87*, 723–729.
- (8) Mirabelli, M. F.; Wolf, J.-C.; Zenobi, R. *Analyst* **2017**, *142*, 1909–1915.
- (9) Käfer, D.; Bashir, A.; Witte, G. *J. Phys. Chem. C* **2007**, *111*, 10546–10551.
- (10) Otto, A.; Akemann, W.; Pucci, A. *Isr. J. Chem.* **2006**, *46*, 307–315.
- (11) Hugall, J. T.; Baumberg, J. J. *Nano Lett.* **2015**, *15*, 2600–2604.
- (12) Xie, X.; Cahill, D. G. *Appl. Phys. Lett.* **2016**, *109*.
- (13) Pozzi, E. A.; Zrimsek, A. B.; Lethiec, C. M.; Schatz, G. C.; Hersam, M. C.; Van Duyne, R. P. *J. Phys. Chem. C* **2015**, *119*, 21116–21124.
- (14) Akemann, W.; Otto, a. *Philos. Mag. Part B* **1994**, *70*, 747–760.

- (15) Pedregosa, F.; Varoquaux, G.; Gramfort, A.; Michel, V.; Thirion, B.; Grisel, O.; Blondel, M.; Prettenhofer, P.; Weiss, R.; Dubourg, V.; et al. *J. Mach. Learn. Res.* **2012**, *12*, 2825–2830.
- (16) Chang, C.; Lin, C. *ACM Trans. Intell. Syst. Technol.* **2013**, *2*, 1–39.
- (17) Fang, Y.; Seong, N.-H.; Dlott, D. D. *Science* **2008**, *321*, 388–392.
- (18) Wadehra, J. M. *Appl. Phys. Lett.* **1979**, *35*, 917–919.
- (19) Christopher, P.; Xin, H.; Linic, S. *Nat. Chem.* **2011**, *3*, 467–472.